



V CONGRESSO NACIONAL DE ENGENHARIA MECÂNICA
V NATIONAL CONGRESS OF MECHANICAL ENGINEERING
25 a 28 de agosto de 2008 – Salvador – Bahia - Brasil
August 25 – 28, 2008 - Salvador – Bahia – Brazil

COMPUTATION OF NON-EQUILIBRIUM HYPERSONIC FLOWFIELD AROUND HYBRID POWER-LAW LEADING EDGE

Wilson F. N. Santos, wilson@lcp.inpe.br

Combustion and Propulsion Laboratory
National Institute for Space Research
Cachoeira Paulista, SP 12630-000

Abstract. *The flowfield structure of a family of hybrid power-law leading edges immersed in high-speed rarefied flow is examined by using the Direct Simulation Monte Carlo (DSMC) method. The work is motivated by interest in assessing the overall performance of power-law leading edges in order to consider them as possible candidates for blunting geometries of hypersonic configurations, since power-law leading edge shapes have characteristics of a sharp body (infinite body slope) and of a blunt body (zero radius of curvature) at the nose. The behavior of the primary properties for asymmetric or hybrid power-law shapes are compared to those for symmetric power-law shapes. The results presented highlight the sensitivity of the velocity, density, pressure and temperature due to changes on the power-law exponent of the upper-surface shape of the leading edges. Interesting features for sharp and blunt leading edges were noted on the computational results of the flowfield structure. It was found that the changes on the upper-surface shape have different influence on velocity, density, pressure and temperature along the stagnation streamline ahead of the leading edges as well as on the profiles adjacent to the body surface.*

Keywords: *DSMC, rarefied flow, hypersonic flow, non-equilibrium flow, power-law shapes.*

1. INTRODUCTION

Waveriders are aerodynamic configurations whose design is based on known supersonic or hypersonic flowfield. Generated by an inverse method from streamlines behind a known shock wave, the waverider lower surface is a stream surface of a known inviscid flow around a reference body, for instance, behind planar oblique shock wave (Nonweiler, 1959), behind conical shock waves around circular or elliptical cones (Rasmussen, 1980, and Kim, Rasmussen and Jischke, 1983), behind power-law shocks (Rasmussen and Duncan, 1995, Mazhul and Rakchimov, 2004, and Mangin et al., 2006), as well as the flows in converging cone ducts (Goonko, Nazhul and Markelov, 2000).

Waverider-based hypersonic vehicle must operate in a wide range of freestream Mach number. When flying at its design Mach number, the entire bow shock is attached to the leading edge of the body. The attached shock wave may prevent spillage of high-pressure airflow from the lower side of the vehicle to the upper side, resulting in a high-pressure differential and enhanced lift. It is the shock attachment that produces de high lift-to-drag (L/D) ratio observed in waverider vehicles.

Nevertheless, at hypersonic flight speeds, the vehicle leading edges should be blunt to some extent in order to reduce the heat transfer rate to acceptable levels and to allow for internal heat conduction. The use of blunt-nose shapes tends to alleviate the aerodynamic heating problem since the heat flux for blunt bodies is far lower than that for sharply pointed bodies. Therefore, due mainly to manufacturing problems and the extremely high temperatures attained in hypersonic flight, hypersonic vehicles should have blunt nose, although probably slendering out at a short distance from the nose. Nonetheless, geometric bluntness results in shock-wave detachment. Thus, the loss of shock-wave attachment will allow pressure leakage from the lower side of the vehicle to the upper side, thereby degrading the aerodynamic performance of waverider vehicle.

In this context, power-law shaped leading edges ($y \propto x^p$, $0 < p < 1$) may provide the required bluntness for heat transfer and manufacturing concerns with less increase in shock-wave detachment so that the final design more closely approximates the ideal aerodynamic performance. This concept is based on work of Mason and Lee (1994) that pointed out, based on Newtonian flow analysis, that these shapes exhibit both blunt and sharp aerodynamic properties. According to them, for values in the range of $0 < p < 1$, the slope of the power-law shape is infinite at $x = 0$, a characteristic of a blunt body. However, for $1/2 < p < 1$, the radius of curvature at the nose approaches zero, a characteristic of a sharp body.

A great deal of experimental and theoretical works has been carried out previously on power-law form representing blunt geometries. Of particular interest are the works by Santos and Lewis (2002, 2005a, and 2005b) and by Santos

(2005, and 2008). The major interest in these works has gone into considering the power-law shape as possible candidate for blunting geometries of hypersonic waverider leading edge.

Santos and Lewis (2002 and 2005b) have investigated power-law shapes in rarefied hypersonic flow through the use of the Direct Simulation Monte Carlo (DSMC) method. They found that the stagnation point heating behavior for power-law leading edges with finite radius of curvature, $p = 1/2$, followed that predicted for classical blunt body in that the heating rate is inversely proportional to the square root of curvature radius at the stagnation point. For those power-law leading edges with zero radii of curvature, $p > 1/2$, it was found that the stagnation point heating is not a function of the curvature radius at the vicinity of the leading edges, but agreed with the classical blunt body behavior predicted by the continuum flow far from the stagnation point. Results were compared to a corresponding circular cylinder to determine which geometry would be better suited as a blunting profile. Their analysis also showed that power-law shapes provided smaller total drag than circular cylinder, typically used in blunting sharp leading edges for heat transfer considerations. However, circular cylinder provided smaller stagnation point heating than power-law shapes under the range of conditions investigated.

In order to assess the advantages and disadvantages of a power-law body, computational results are obtained for a different scenario of power-law shapes. In the present account, the flowfield structure is investigated for hybrid power-law shapes, i.e., lower and upper surfaces with different power-law exponents. In this connection, the purpose of this work is to examine computationally the shape effects on the primary properties of asymmetric or hybrid power-law leading edges in order to provide information on how well these shapes stand up as possible candidates for blunting geometries of hypersonic leading edges. The impact on upstream and adjacent property profiles due to changes on the leading-edge shape will be investigated for a combination of power-law exponents of $1/2$, $3/5$, $2/3$ and $3/4$ for the upper and lower surface shapes.

2. LEADING-EDGE GEOMETRY

In dimensional form, the body power-law shapes are given by the following expression,

$$y = Ax^p \tag{1}$$

where p is the power-law exponent and A is the power-law constant, which is a function of p .

In the previous work (Santos and Lewis, 2002), the symmetric power-law shapes were modeled by assuming a sharp-edged wedge of half angle θ with a circular cylinder of radius R inscribed tangent to this wedge. The power-law shapes, inscribed between the wedge and the cylinder, are also tangent to them at the same common point where they have the same slope angle. The circular cylinder diameter provides a reference for the amount of blunting desired on the leading edges. It was assumed a leading-edge half angle of 10 degrees, a circular cylinder diameter of 10^{-2} m and power-law exponents of $1/2$, $3/5$, $2/3$, $7/10$, $3/4$, and $4/5$. Figure (1a) illustrates schematically this construction for the set of symmetric power-law leading edges previously investigated.

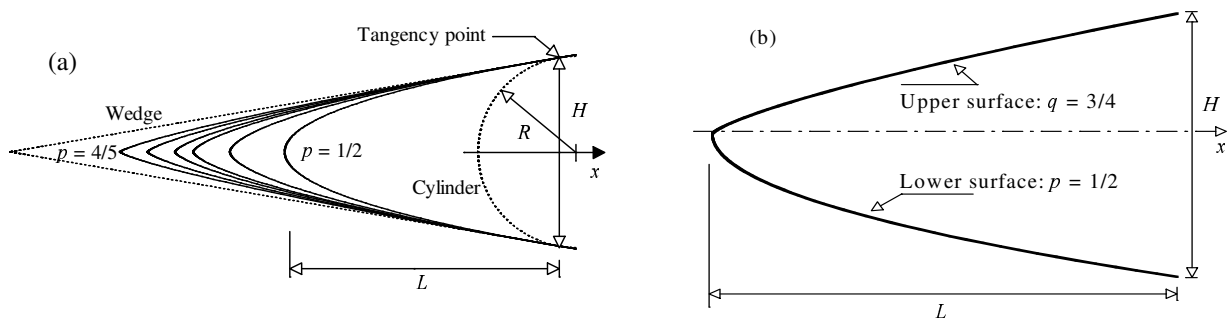


Figure 1: Drawing illustrating the (a) symmetric and (b) the asymmetric power-law leading edges.

From geometric considerations, the common body height H , Fig. (1a), at the tangency point is equal to $2R\cos\theta$. The power-law constant A , obtained by matching slope on the wedge, circular cylinder and power-law body at the tangency point is given as follows,

$$A = \frac{\left(\frac{R^2}{1 + \tan^2 \theta} \right)^{(1-p)/2}}{\left(\frac{p}{\tan \theta} \right)^p} \tag{2}$$

As the slope of the power-law shapes is infinite at $x = 0$, i.e., the slope angle is 90 degrees, the asymmetric or

hybrid power-law shapes were obtained by combining the upper and lower part of the curves, with respect to the symmetry line, shown in Fig. (1a). In this way, for the hybrid power-law shapes, the upper surface was represented by the exponent q of $3/5$, $2/3$ or $3/4$ and the lower surface by the exponent p of $1/2$. Figure (1b) illustrates an asymmetric or hybrid power-law leading edge defined by $q = 3/4$ and $p = 1/2$. It was assumed that the hybrid power-law leading edges are infinitely long but only the length L is considered in the simulation since the wake region behind the power-law bodies is not of interest in this investigation.

3. COMPUTATIONAL METHOD

The choice of the numerical approach to be used to model rarefied non-equilibrium flows greatly relies on the extent of flow rarefaction. For near-continuum flows, it is usually sufficient to take into account the effects of rarefaction through the boundary conditions of slip velocity and temperature jump on the surface. The Navier-Stokes equations, commonly used with these boundary conditions, can be derived from the transport Boltzmann equation under the assumption of small deviation of the distribution function from equilibrium. Nevertheless, the Navier-Stokes equations became unsuitable for studying rarefied flows where the distribution function becomes considerable in non-equilibrium.

In order to study rarefied flow with a significant degree of non-equilibrium, the Direct Simulation Monte Carlo (DSMC) method (Bird, 1994) is usually employed. The DSMC method has become the most common computational technique for modeling complex transitional flows of engineering interest. The DSMC method model a gas flow by using a computer to track the trajectory of simulated particles, where each simulated particle represents a fixed number of real gas particles. The simulated particles are allowed to move and collide, while the computer stores their position coordinates, velocities and other physical properties such as internal energy. The simulation is always calculated as unsteady flow. However, a steady flow solution is obtained as the large time state of the simulation.

The molecular collisions are modeled by using the variable hard sphere (VHS) molecular model (Bird, 1981) and the no time counter (NTC) collision sampling technique (Bird, 1989). The energy exchange between kinetic and internal modes is controlled by the Borgnakke-Larsen statistical model (Borgnakke and Larsen, 1975). Simulations are performed using a non-reacting gas model consisting of two chemical species, N_2 and O_2 . Energy exchanges between the translational and internal modes, rotational and vibrational, are considered. For a given collision, the probabilities are designated by the inverse of the relaxation numbers, which correspond to the number of collisions necessary, on average, for a molecule to relax. Relaxation collision numbers of 5 and 50 were used for the calculations of rotation and vibration, respectively.

4. COMPUTATIONAL DOMAIN AND GRID

In order to implement the particle-particle collisions, the flowfield is divided into an arbitrary number of regions, which are subdivided into computational cells. The cells are further subdivided into four subcells, two subcells/cell in each direction. The cell provides a convenient reference sampling of the macroscopic gas properties, whereas the collision partners are selected from the same subcell for the establishment of the collision rate. As a result, the flow resolution is much higher than the cell resolution. The dimensions of the cells must be such that the change in flow properties across each cell is small. The linear dimensions of the cells should be small in comparison with the distance over which there is a significant change in the flow properties. These conditions define that the cell dimensions should be of the order of the local mean free path or even smaller (Bird, 1994).

The computational domain used for the calculation is made large enough so that body disturbances do not reach the upstream and side boundaries, where freestream conditions are specified. A schematic view of the computational domain is depicted in Fig. (2). Side I is defined by the body surface. Diffuse reflection with complete thermal accommodation is the condition applied to this side. Side II is the freestream side through which simulated molecules enter and exit. Finally, side III is the downstream outflow boundary. At this boundary, the flow is predominantly supersonic and vacuum condition is specified (Bird, 1994). As a result, it is assumed that at this boundary simulated molecules can only exit.

The effects of grid resolution and the effects of the number of particles per computational cell were investigated in order to determine the number of cells and the number of particles required to achieve grid independence solutions. In this fashion, a grid independence study was made with three different structured meshes in each coordinate direction. The effect of altering the cell size in the ξ -direction was investigated with grids of 60(coarse), 90(standard) and 120(fine) cells on the upper and lower surfaces, and 60 cells in the η -direction for the leading edges investigated. In analogous manner, an examination was made in the η -direction with grids of 30(coarse), 60(standard) and 90(fine) cells, and 90 cells along the upper and lower surface, i.e., in the ξ -direction. In addition, each grid was made up of non-uniform cell spacing in both directions. The effect (not shown) of changing the cell size in

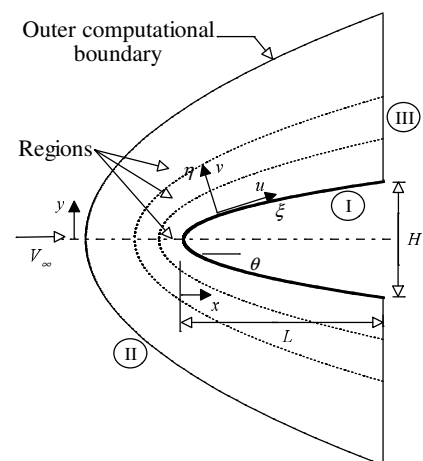


Figure 2: Drawing illustrating the computational domain.

both directions on the heat transfer and pressure coefficients was rather insensitive to the range of cell spacing considered, indicating that the standard grid, 180x60 cells in the entire domain is essentially grid independent. A similar procedure was performed with respect to the number of particles. The total number of particles depends on the case investigated. On the average, it is around of 350,000 particles.

5. COMPUTATIONAL CONDITIONS

DSMC simulations have been performed based on the flow conditions given by Santos and Lewis (2002) and summarized in Tab. (1), and the gas properties (Bird, 1994) are shown in Tab. (2).

Table 1: Freestream Conditions

Temperature T_∞ (K)	Pressure p_∞ (N/m ²)	Density ρ_∞ (kg/m ³)	Number density n_∞ (m ⁻³)	Viscosity μ_∞ (Ns/m ²)	Mean free path λ_∞ (m)
220.0	5.582	8.753×10^{-5}	1.8209×10^{21}	1.455×10^{-5}	9.03×10^{-4}

Table 2: Gas Properties

	Mole fraction X	Molecular mass m (kg)	Molecular diameter d (m)	Viscosity Index ω
O ₂	0.237	5.312×10^{-26}	4.01×10^{-10}	0.77
N ₂	0.763	4.65×10^{-26}	4.11×10^{-10}	0.74

The freestream velocity V_∞ is assumed to be constant at 3.56 km/s. This velocity corresponds to a freestream Mach number M_∞ of 12. The translational and vibrational temperatures in the freestream are in equilibrium at 220 K. The wall temperature T_w is assumed constant at 880 K. This temperature is chosen to be representative of the surface temperature near the stagnation point and is assumed to be uniform over the entire surface of the leading edges.

The freestream Knudsen number Kn_∞ , defined as the ratio of the molecular mean free path λ in the freestream gas to a characteristic dimension of the flowfield, corresponds to 0.0903, where the characteristic dimension was defined as being the diameter of the reference circular cylinder (see Fig. (1)). The freestream Reynolds number Re_∞ by unit meter is 21,455.

In order to simulate the shape effects, the DSMC calculations were performed independently for a family of hybrid power-law leading edges. The upper surface shape, represented by the exponent q , assumed the values 1/2, 3/5, 2/3 and 3/4, and the lower surface shape, referred by the exponent p , was fixed at 1/2. It should be mentioned in this context that the leading edge defined by $p = q = 1/2$ represents the symmetric power-law leading edge investigated previously by Santos and Lewis (2002).

6. COMPUTATIONAL RESULTS AND DISCUSSION

The purpose of this section is to discuss and to compare differences in the flowfield properties due to variations on the leading-edge shape. The flowfield properties of particular interest in the regime of intermediate Knudsen number are velocity, density, pressure and temperature.

6.1. Velocity Profiles

Normal velocity profiles upstream the leading edges and their dependence on the power-law exponent are illustrated in Figs. (3a), (3b) and (3c), for power-law exponent q of 3/5, 2/3, and 3/4, respectively. In this set of plots, the velocity ratio represents the normal velocity v normalized by the freestream velocity V_∞ , the dimensionless height stands for the height y , normal to the stagnation line of the leading edges, normalized by the freestream mean free path λ_∞ , and X represents the upstream length x along the stagnation line of the leading edges also normalized by λ_∞ . In addition, p and q refer to the power-law exponents of the lower and upper surfaces, respectively.

According to Figs. (3a), (3b) and (3c), it is clearly noted that the velocity profiles are asymmetric about the centerline for the cases shown. As the power-law exponent q increases, the profiles become much more asymmetric and the minimum value on the profiles occurs below the centerline. As a base of comparison, at station $X = -0.001$, the normal velocity reaches 99% of the freestream velocity V_∞ at $8.74\lambda_\infty$, $7.95\lambda_\infty$ and $7.26\lambda_\infty$ above the centerline for power-law shapes defined by q of 3/5, 2/3 and 3/4, respectively. In contrast, below the centerline, $0.99 V_\infty$ is reached at $-9.79\lambda_\infty$, $-9.63\lambda_\infty$ and $-9.39\lambda_\infty$, respectively, for the same leading edges. Consequently, changes on the upper-surface shape modify the velocity profiles on the lower side of the leading edges. The reason for that is because as the power-law exponent increases on the upper-surface shape the leading edge becomes sharp and more streamlined on the upper part than that on the lower part of the leading edge for the oncoming freestream molecules. It is also noted that the velocity profile at station $X = -5.0$ is not affected anymore by the presence of the leading edges.

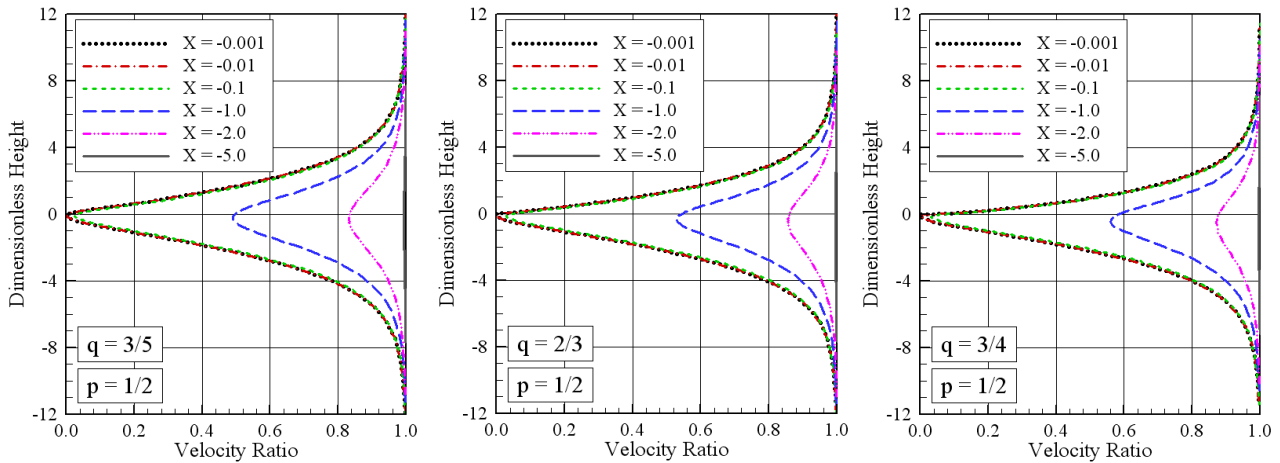


Figure 3: Normal velocity (v/V_∞) profiles upstream of the power-law leading edges corresponding to lower-surface shape of $p = 1/2$ and upper-surface shape q of (a) 3/5, (b) 2/3 and (c) 3/4.

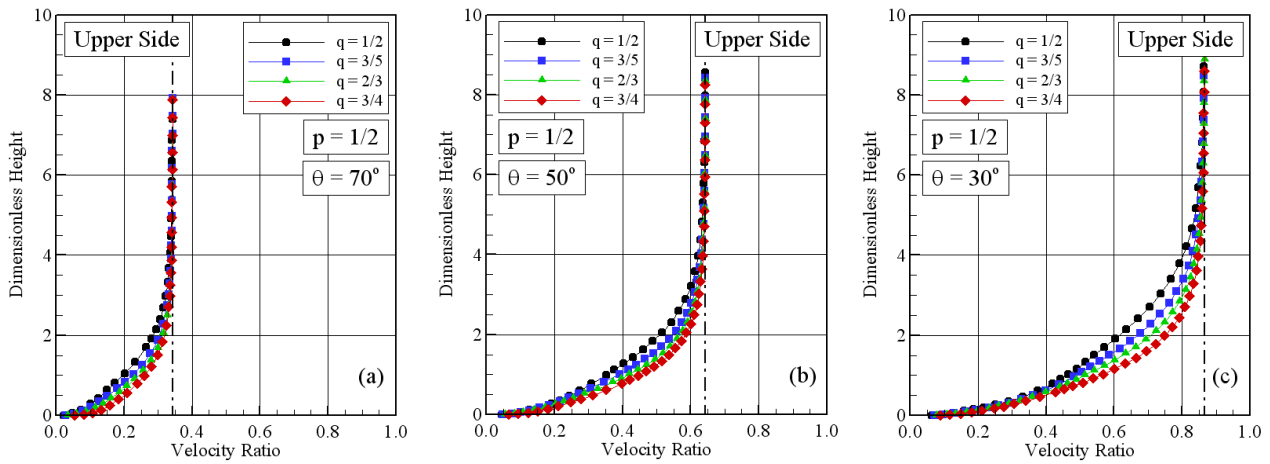


Figure 4: Tangential velocity (u/V_∞) profiles along the body upper surface as a function of the power-law exponent at stations corresponding to body slope angle of (a) 70, (b) 50 and (c) 30 degrees.

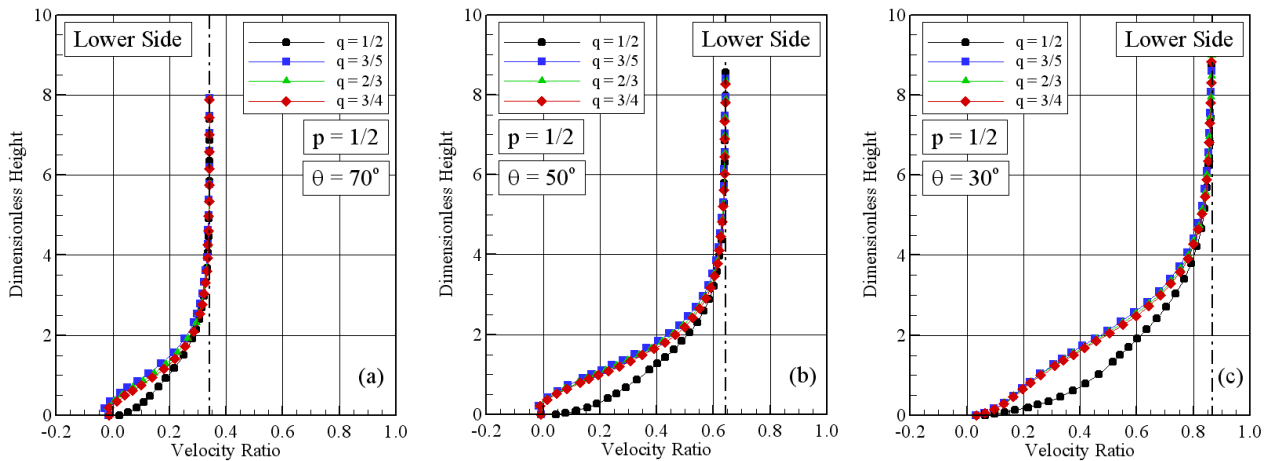


Figure 5: Tangential velocity (u/V_∞) profiles along the body lower surface as a function of the power-law exponent at stations corresponding to body slope angle of (a) 70, (b) 50 and (c) 30 degrees.

The outer extent of the flowfield disturbance over the upper and lower body surfaces is demonstrated in Figs. (4) and (5), respectively, as a function of the power-law exponent q . In these figures, the velocity ratio stands for the tangential velocity u normalized by the freestream velocity V_∞ and the dimensionless height represents the height η in the off-body direction (η -direction in Fig. (2)) normalized by λ_∞ . In an effort to emphasize points of interest, this set of plots presents data for three stations along the body surface that correspond to the body slope angle of 70, 50 and 30

degrees. It is important to mention that these slope angles are equivalent to different arc length s/λ_∞ not only on the upper side but also on the lower side for the leading edges investigated. For comparison purpose, tangential velocity profile for the symmetric case of $p = q = 1/2$ is also shown in the plots.

Interesting features can be drawn from this set of tangential velocity profiles. As the body slope decreases the tangential velocity adjacent to the body surface increases. This is to be expected since the flow experiences an expansion as it moves downstream along the body surface. It is observed that the flow accelerates faster on the upper surface by increasing the power-law exponent q . With increasing the power-law exponent of the upper-surface shape, the flow behavior at the vicinity of the leading edges changes aerodynamically from blunt to sharp one. As a result, the tangential velocity increases since the sharp shape causes a smaller disturbance in the flowfield. It should be noted that the tangential velocity u_∞ defined as $\eta \rightarrow \infty$, is represented by the dashed line and shown for each station. Because of the body curvature, $u_\infty (\equiv V_\infty \cos\theta)$ varies as a function of the body slope.

Still referring to Figs. (4) and (5), it is encouraging to observe that significant differences in the velocity profiles along the upper and lower sides occur adjacent to the body surface. Of great significance in this set of figures is the slip velocity. It is seen that slip velocity increases on the upper side and on the lower side of the leading edge with increasing the power-law exponent q . In addition, as indeed is clear from these figures, there is backflow on the lower side of the body surface for the stations defined by body slope angles of 70 and 50 degrees.

6.2. Density Profiles

Density profiles at six axial locations upstream the leading edges are plotted as a function of the power-law exponent q in Fig. (6). In this set of plots, density ratio stands for density ρ normalized by the freestream density ρ_∞ .

According to Figs. (6a), (6b) and (6c), it is seen that the density profiles follow the same trend of those for velocity profiles in the sense that they are clearly asymmetric with respect to the centerline. Of great significance is the density ratio value at the stagnation point, for instance at station $X = -0.001$. It is noteworthy that density rises to well above the continuum inviscid limit. As a point of reference, the Rankine-Hugoniot relations give a postshock density that corresponds to the ratio $\rho/\rho_\infty = 5.8$ for freestream Mach number of 12. Near the stagnation point, $X = -0.001$, the pick value for density ρ is around 20, 19 and 18 times the freestream density ρ_∞ for leading edges defined by power-law exponent q of 3/5, 2/3 and 3/4, respectively. The substantial density increase above the freestream density value is a characteristic of cold-wall entry flow. In typical entry flow, the body surface temperature is low compared to the stagnation temperature. This leads to a steep density gradient near the body surface. For the present simulation, the ratio of wall temperature to stagnation temperature is 0.13, which corresponds to a cold-wall flow. On the other hand, the density reduction due to changes on the upper-surface shape is explained by the fact that the leading edge becomes aerodynamically sharp with the power-law exponent rise.

It is also noted that the density profile at station $X = -2.0$ is not affected anymore by the presence of the leading edges. This is in contrast to the velocity profiles that was not affected anymore for station $X = -5.0$. Therefore, the upstream disturbance domain for density is smaller than that for normal velocity.

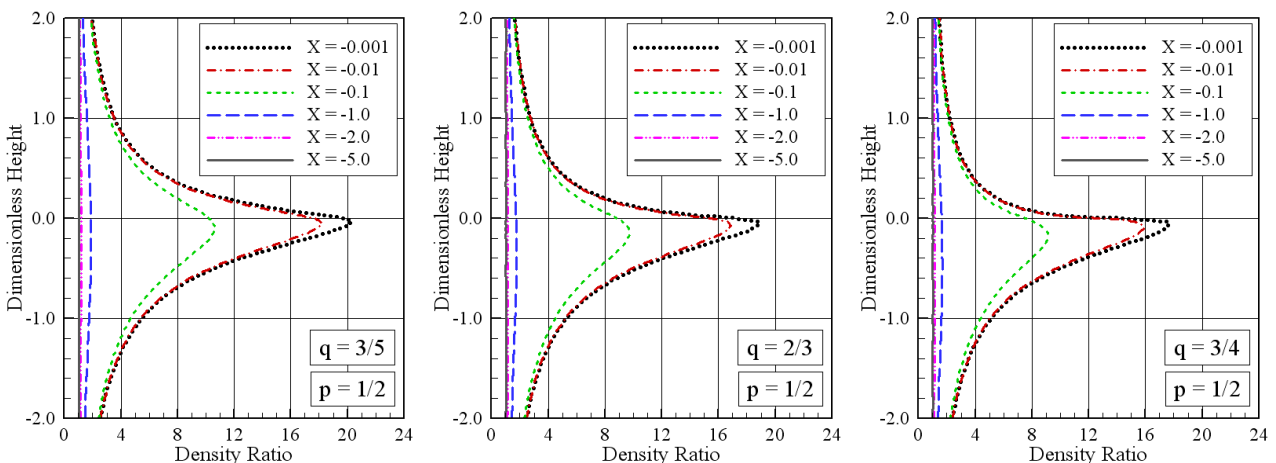


Figure 6: Density (ρ/ρ_∞) ratio profiles upstream of the power-law leading edges corresponding to lower-surface shape of $p = 1/2$ and upper-surface shape q of (a) 3/5, (b) 2/3 and (c) 3/4.

Selected profiles of the local density, expressed as a ratio to the freestream value ρ_∞ are displayed in Figs. (7) and (8) for three stations located on the upper and lower surfaces, respectively. Again, for comparison purpose, density profile for the symmetric case of $p = q = 1/2$ is shown in the plots.

Looking first at Figs. (7a), (7b) and (7c), it is seen that the density along the body surface experiences significant changes with the flow expansion as the flow moves downstream. As would be expected, these changes are related to the shape of the leading edges. Density is high at the vicinity of the stagnation region and decreases downstream along the

body surface. For instance, for the station corresponding to 70 degrees, Fig. (7a), the density variation is in excess of one order of magnitude in comparison to the freestream density for the leading edge investigated. In this region, the compression combined with a relatively cool wall produces a maximum density that is around 18, 16 and 14 times the freestream density value for power-law exponent q of 3/5, 2/3 and 3/4, respectively. Because of the flow expansion along the body surface, the density adjacent to the body surface decreases to around 11, 10 and 9 times the freestream value at the station corresponding to 30 degrees, as shown in Fig. (7c), a reduction around 60%.

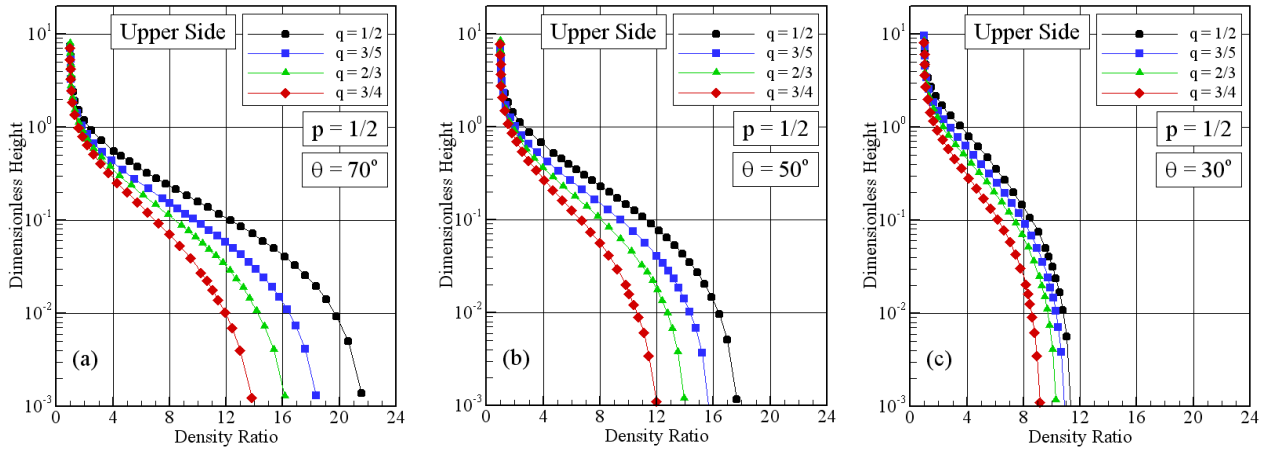


Figure 7: Density (ρ/ρ_∞) ratio profiles along the body upper surface as a function of the power-law exponent at stations corresponding to body slope angle of (a) 70, (b) 50 and (c) 30 degrees.

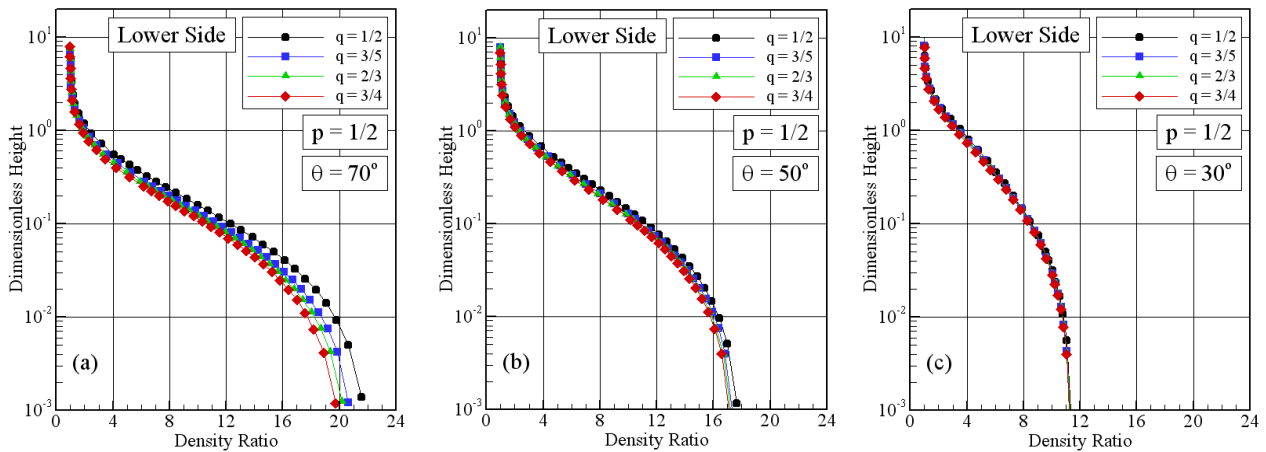


Figure 8: Density (ρ/ρ_∞) ratio profiles along the body lower surface as a function of the power-law exponent at stations corresponding to body slope angle of (a) 70, (b) 50 and (c) 30 degrees.

Turning next to Figs. (8a), (8b) and (8c), it is also noticed that changes on the upper-surface shape causes a smaller effect on the density distribution on the lower surface than that on the upper surface. At station corresponding to 70 degrees, it is observed that density profiles are affected for variations on the upper-surface shape. Nevertheless, no effect is observed on the density profiles for station corresponding to body slope angle of 30 degrees, Fig. (8c), where all leading edges present basically the same density ratio value.

It may be observed from Figs. (7) and (8) that density also experiences significant changes in the direction perpendicular to the wall (η -direction) as the flow moves downstream along the body surface. In the η -direction, the density is high adjacent to the wall and rapidly decreases inside a layer of thickness around one freestream mean free path λ_∞ , where the density approaches the freestream density value for the leading edges investigated. This characteristic is observed when the body surface is very much colder than the stagnation temperature of the oncoming gas. As a result, the gas near to the body tends to be much denser and cooler than the gas in the rest of the boundary layer.

6.3. Pressure Profiles

The large amount of kinetic energy present in a hypersonic freestream is converted by molecular collisions into high thermal energy surrounding the body and by flow work into increased pressure. In this respect, the stagnation line

is a zone of strong compression, where pressure increases from the freestream to the stagnation point due to the shock wave that forms ahead of the leading edges.

Representative pressure profiles upstream the leading edges are displayed as a function of the power-law exponent q in Figs. (9a), (9b) and (9c) for power-law exponent q of $3/5$, $2/3$ and $3/4$, respectively. In this set of diagrams, pressure ratio stands for pressure p normalized by the freestream pressure p_∞ .

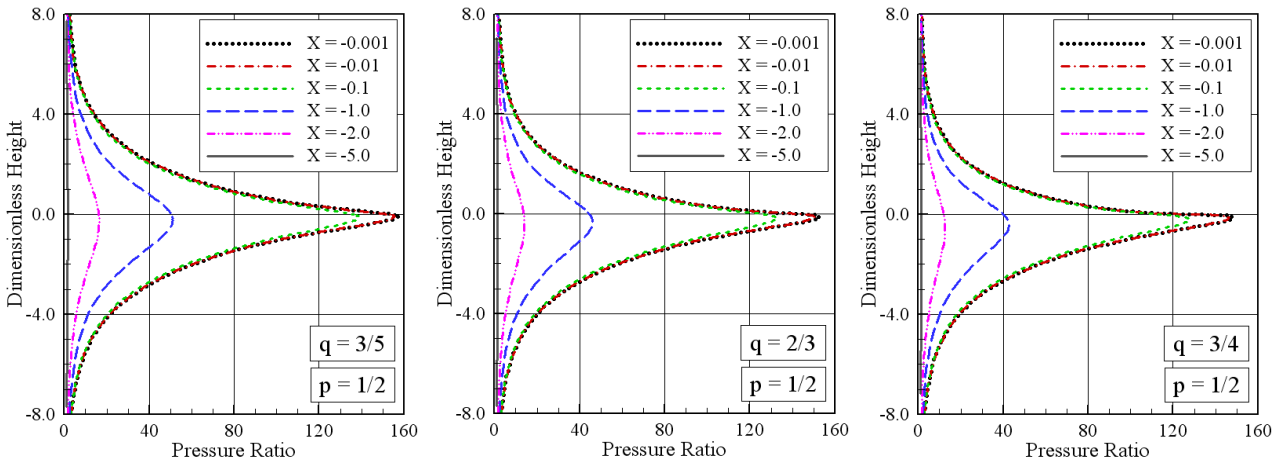


Figure 9: Pressure (p/p_∞) ratio profiles upstream of the power-law leading edges corresponding to lower-surface shape of $p = 1/2$ and upper-surface shape q of (a) $3/5$, (b) $2/3$ and (c) $3/4$.

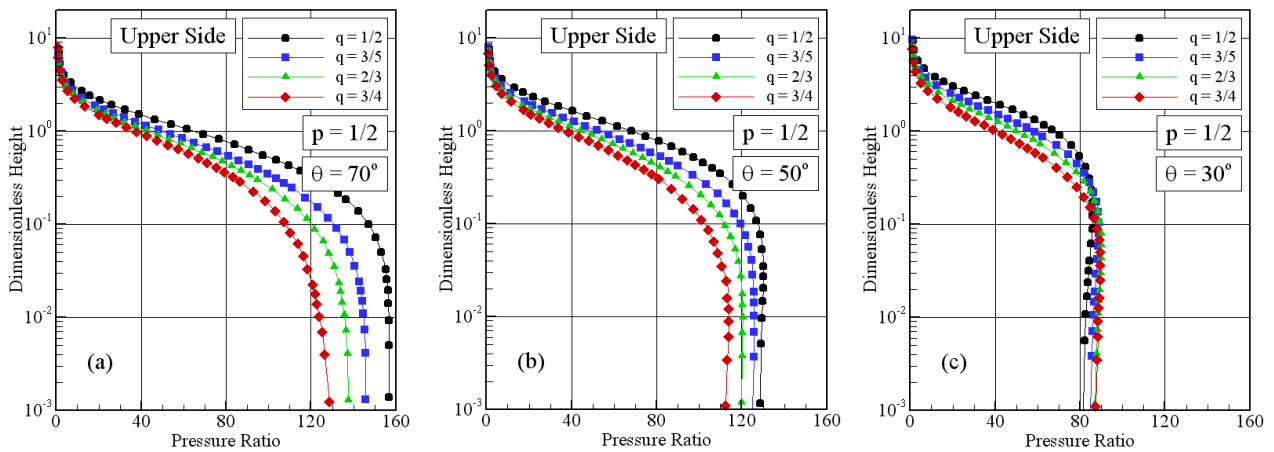


Figure 10: Pressure (p/p_∞) ratio profiles along the body upper surface as a function of the power-law exponent at stations corresponding to body slope angle of (a) 70° , (b) 50° and (c) 30° degrees.

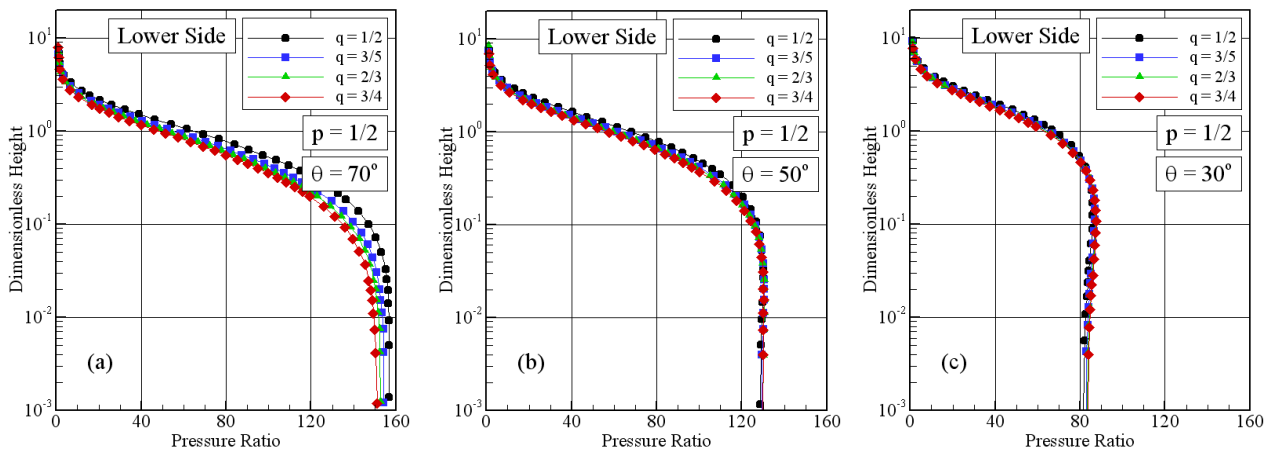


Figure 11: Pressure (p/p_∞) ratio profiles along the body lower surface as a function of the power-law exponent at stations corresponding to body slope angle of (a) 70° , (b) 50° and (c) 30° degrees.

According to Figs. (9a), (9b) and (9c), it is observed that the upper-surface shape effects on pressure profiles are similar to those observed on density profiles. As would be expected, the profiles are asymmetric with respect to the centerline, and the asymmetry increases with increasing the power-law exponent q . In addition, the pick value for pressure p takes place at the vicinity of the stagnation region and decreases in the upstream direction. Of particular interest in this set of plots is the upstream disturbance effect. As can be noticed, pressure profile at station $X = -2.0$ is still affected by the presence of the leading edge.

In what follows, local pressure for three stations located on the upper and lower surfaces are provided, respectively, for Figs. (10) and (11). From these profiles, it is firmly established that meaningful changes occur on the pressure due to the flow expansion along the body surface. As an illustrative example, for body slope angle of 70 degrees, the pressure variation is in excess of two orders of magnitude with respect to p_∞ for the leading edges investigated. In this region, close to the stagnation region, the compression produces a maximum pressure that is above 120 times the freestream pressure value for the cases shown. Due to the flow expansion along the body surface, the pressure adjacent to the surface decreases to around 80 times the freestream pressure value at the body slope angle of 30 degrees.

6.4. Temperature Profiles

Kinetic temperature profiles along the stagnation streamline are demonstrated in Fig. (12). In this figure, translational temperature T_T , rotational temperature T_R , vibrational temperature T_V and the overall temperature T_{OV} are normalized by the freestream temperature T_∞ . Also, X represents the upstream length x along the stagnation line of the leading edges normalized by λ_∞ . In addition, filled and empty symbols stand for leading-edge shapes defined by q of 3/5 and 3/4, respectively. It is apparent from this figure that thermodynamic non-equilibrium occurs throughout the shock layer, as shown by the lack of equilibrium of the translational and internal kinetic temperatures. Thermal non-equilibrium occurs when the temperatures associated with the translational, rotational, and vibrational modes of a polyatomic gas are different. In this scenario, it proves convenient to define the overall kinetic temperature, obtained for a non-equilibrium gas as the weighted mean of the translational and internal temperatures. The overall kinetic temperature is equivalent to the thermodynamic temperature only under thermal equilibrium conditions. It should be remarked that the ideal gas equation of state does not apply to this temperature in a non-equilibrium situation.

It may be recognized from Fig. (12) that, in the undisturbed freestream far from the body, the translational and internal temperatures have the same value and are equal to the thermodynamic temperature. Approaching the nose of the leading edges, the translational temperature rises to well above the rotational and vibrational temperatures and reaches a maximum value that is a function of the leading-edge shape. Since a large number of collisions is needed to excite molecules vibrationally from the ground state to the upper state, the vibrational temperature increases more slowly than rotational temperature. Still further downstream toward the nose of the leading edges, the translational temperature decreases and reaches a value at the stagnation point that is still above the wall temperature, resulting in a temperature jump as defined in continuum formulation.

Still referring to Fig. (12), it is noticed that changes on the upper-surface shape affect the kinetic temperature profiles. By increasing the power-law exponent q , the pick value for the translational temperature decreases and moves to the stagnation point direction. This is explained by the fact that the leading edge becomes sharper with increasing q .

For the time being, it is instructive to explore the upstream disturbance effects on the overall kinetic temperature caused by variations on the upper-surface shape. In this way, overall temperature ratio profiles at six locations upstream the nose of the leading edges are demonstrated as a function of the power-law exponent q in Fig. (13).

Interesting features may be recognized from Figs. (13a), (13b) and (13c). It is clearly seen that, at the stagnation point, at station $X = -0.001$, the pick value for overall temperature takes place above and below the centerline. Nevertheless, at station $X = -1.0$, the maximum value for overall temperature is located close to the centerline. In addition, the pick value increases with decreasing the power-law exponent q . This is in agreement with the temperature profiles shown in Fig. (12). This behavior is explained by the fact that, by decreasing the power-law exponent q the leading edge becomes blunt. For blunt body, molecules reflecting from the nose region collide with those oncoming freestream molecules, therefore high-velocity molecules. Consequently, the large velocity separation between these two classes of molecules results in a temperature rise far from the nose.

In the following, particular attention is paid to the overall kinetic temperature in the shock layer. In this respect, the overall kinetic temperature variation is taken normal to the body surface at body stations corresponding to 70, 50, and 30 degrees. Figures (14) and (15) depict profiles of overall kinetic temperatures on the upper and lower surfaces, respectively, as a function of the power-law exponent q at the considered positions. According to this set of plots, it is observed that the downstream evolution of the flow displays a smearing tendency of the shock wave due to the displacement of the maximum value for the overall kinetic temperature. Also, it may be recognized from the overall

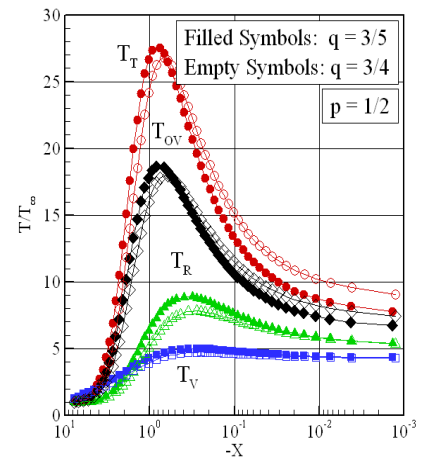


Figure 12: Kinetic temperature (T/T_∞) profiles along the stagnation streamline as a function of the power-law exponent q .

temperature distributions that significant changes in the overall kinetic temperature profiles occur within a larger layer adjacent to the body surface compared to that for either density or pressure. It is very encouraging to observe that, by increasing the power-law exponent q , the overall temperature on the upper surface is larger than that for the symmetric power-law leading edge. However, no significant effect is observed in the profiles on the lower surface. In general, this behavior is in contrast to that presented by density and pressure profiles.

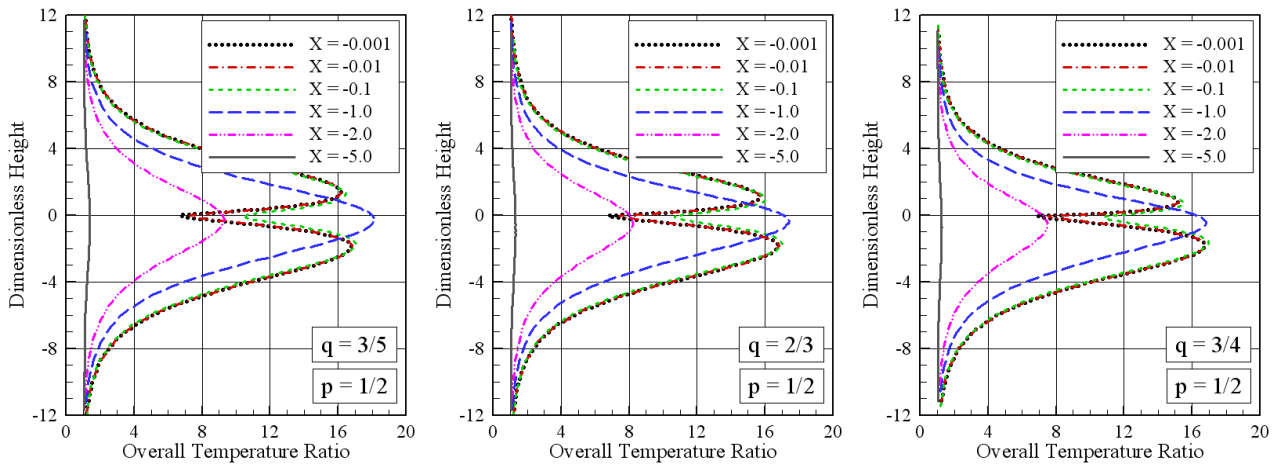


Figure 13: Overall kinetic temperature (T_{OV}/T_{∞}) ratio profiles upstream of the power-law leading edges corresponding to lower-surface shape of $p = 1/2$ and upper-surface shape q of (a) $3/5$, (b) $2/3$ and (c) $3/4$.

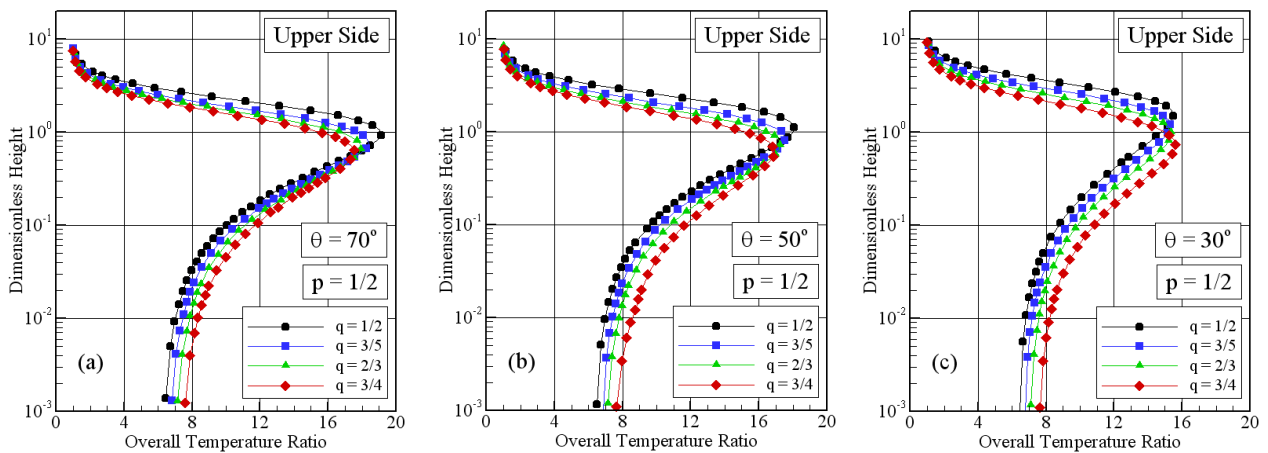


Figure 14: Overall kinetic temperature (T_{OV}/T_{∞}) ratio profiles along the body upper surface as a function of the power-law exponent at stations corresponding to body slope angle of (a) 70° , (b) 50° and (c) 30° degrees.

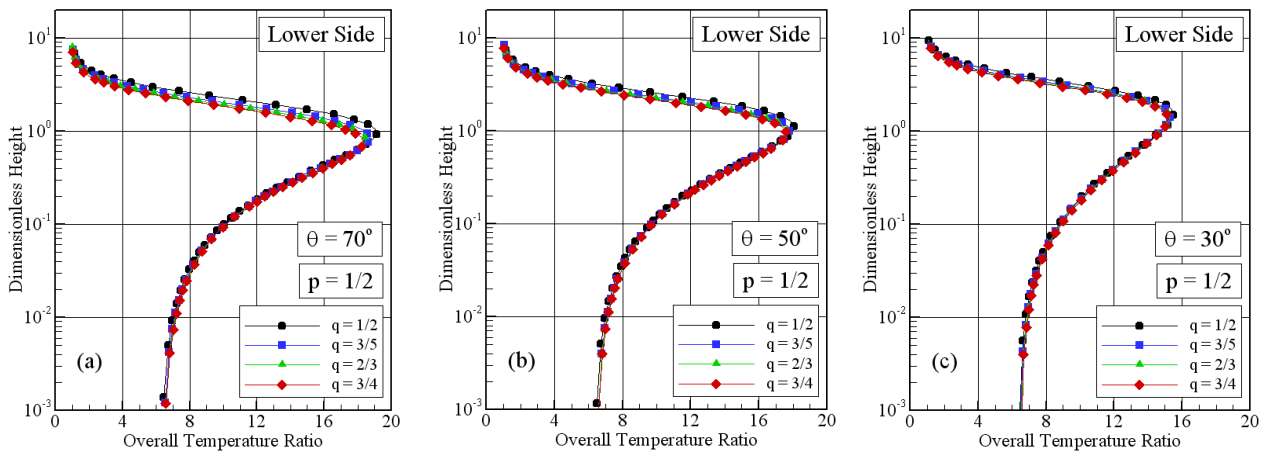


Figure 15: Overall kinetic temperature (T_{OV}/T_{∞}) ratio profiles along the body lower surface as a function of the power-law exponent at stations corresponding to body slope angle of (a) 70° , (b) 50° and (c) 30° degrees.

7. CONCLUDING REMARKS

Computations of a rarefied hypersonic flow on power-law leading edges have been performed by using the Direct Simulation Monte Carlo method. The calculations provided information concerning the nature of the flowfield structure, by means of the primary properties, at the vicinity of the nose and immediately adjacent to the body surface for a family of contours composed by lower and upper surfaces with different power-law exponents. The emphasis of the investigation was to compare symmetric power-law leading edges with asymmetric power-law leading edges in order to determine which geometry is better suited as a blunting profile for hypersonic configurations.

Leading-edge shape effects on the velocity, density, pressure, and temperature for a representative range of parameters were investigated. In this fashion, the upper-surface shape was represented by power-law exponents of 1/2, 3/5, 2/3 and 3/4, and the lower-surface shape was defined by exponent of 1/2.

The analysis showed that changes on the upper-surface shape affected the flowfield structure around the leading edges when compared to that for symmetric power-law leading edges. It was found that changes on the upper-surface shape disturbed the flowfield far upstream, as compared to the freestream mean free path, and the domain of influence decreased by increasing the power-law exponent of the upper-surface shape. Moreover, the extent of the upstream flowfield disturbance is significantly different for each one of the flow properties. The domain of influence for temperature is larger than that observed for pressure and density.

Since the extent of the flowfield disturbance is significantly different for each one of the leading edge shapes, this will have important implications in problems that take into account for the gas-phase chemistry and for the gas-surface catalytic activity.

8. REFERENCES

- Bird, G. A., 1981, "Monte Carlo Simulation in an Engineering Context", Progress in Astronautics and Aeronautics: Rarefied gas Dynamics, Vol. 74, part I, AIAA New York, pp. 239-255.
- Bird, G. A., 1989, "Perception of Numerical Method in Rarefied Gasdynamics", Rarefied gas Dynamics: Theoretical and Computational Techniques, Vol. 118, AIAA, New York, pp. 374-395.
- Bird, G. A., 1994, "Molecular Gas Dynamics and the Direct Simulation of Gas Flows", Oxford University Press, Oxford, England, UK.
- Borgnakke, C. and Larsen, P. S., 1975, "Statistical Collision Model for Monte Carlo Simulation of Polyatomic Gas Mixture", Journal of computational Physics, Vol. 18, No. 4, pp. 405-420.
- Goonko, Y. P., Mazhul, I. I., and Markelov, G. N., 2000, "Convergent-Flow-Derived Waveriders", Journal of Aircraft, Vol. 37, No. 4, pp. 647-654.
- Kim, B. S., Rasmussen, M. L., and Jischke, M. C., 1983, "Optimization of Waverider Configurations Generated from Axisymmetric Conical Flows", Journal of Spacecraft and Rockets, Vol. 20, No. 5, pp. 461-469.
- Mangin, B., Benay, R., Chanetz, B., and Chpoun, A., 2006, "Optimization of Viscous Waveriders Derived from Axisymmetric Power-Law Blunt Body Flows", Journal of Spacecraft and Rockets, Vol. 43, No. 5, pp. 990-998.
- Mason, W. H. and Lee, J., 1994, "Aerodynamically Blunt and Sharp Bodies", Journal of Spacecraft and Rockets, Vol. 31, No. 3, pp. 378-382.
- Mazhul, I. I., and Rackchimov, R. D., 2004, "Hypersonic Power-Law Shaped Waveriders in Off-Design Regimes", Journal of Aircraft, Vol. 41, No. 4, pp. 839-845.
- Nonweiler, T. R. F., 1959, "Aerodynamic Problems of Manned Space Vehicles", Journal of the Royal Aeronautical Society, Vol. 63, Sept, pp. 521-528.
- Rasmussen, M. L., 1980, "Waverider Configurations Derived from Inclined Circular and Elliptic Cones", Journal of Spacecraft and Rockets, Vol. 17, No. 6, pp. 537-545.
- Rasmussen, M. L., and Ducan, B., 1995, "Hypersonic Waveriders Generated from Power-Law Shocks", AIAA Paper 95-6160.
- Santos, W. F. N., and Lewis, M. J., 2002, "Power-Law Shaped Leading Edges in Rarefied Hypersonic Flow", Journal of Spacecraft and Rockets, Vol. 39, No. 6, pp. 917-925.
- Santos, W. F. N., and Lewis, M. J., 2005a, "Calculation of Shock Wave Structure over Power-Law Bodies in Hypersonic Flow", Journal of Spacecraft and Rockets, Vol. 42, No. 2, pp. 213-222.
- Santos, W. F. N., and Lewis, M. J., 2005b, "Aerothermodynamic Performance Analysis of Hypersonic Flow on Power-Law Leading Edges", Journal of Spacecraft and Rockets, Vol. 42, No. 4, pp. 588-597.
- Santos, W. F. N., 2005, "Leading-edge Bluntness Effects on Aerodynamic Heating and Drag of Power Law Body in Low-Density Hypersonic Flow", Journal of the Society of Mechanical Sciences and Engineering, Vol. 27, No. 3, pp. 236-241.
- Santos, W. F. N., 2008, "Physical and Computational Aspects of Shock Waves over Power-Law Leading Edges", Physics of Fluids, Vol. 20, No. 1, pp. 1070631-11.

9. RESPONSIBILITY NOTICE

The author is the only responsible for the printed material included in this paper.